Available online at www.sciencedirect.com
SCIENCE DIRECT®
Earth and Planetary Science Letters 243 (2006) 771 – 785
EPSL
www.elsevier.com/locate/epsl

Flow and fracturing of viscoelastic media under diffusion-driven bubble growth: An analogue experiment for eruptive volcanic conduits

J. Taddeucci [a,b,*], O. Spieler [a], M. Ichihara [c], D.B. Dingwell [a], P. Scarlato [b]

[a] *Department of Earth and Environmental Sciences, University of Munich, Munich, Germany*
[b] *HP-HT Lab, Department of Seismology and Tectonophysics, INGV, Rome, Italy*
[c] *Earthquake Research Institute, University of Tokyo, Tokyo, Japan*

Received 9 June 2005; received in revised form 6 January 2006; accepted 9 January 2006
Available online 17 February 2006
Editor: K. Farley

Abstract

To visualize the behavior of erupting magma in volcanic conduits, we performed shock tube experiments on the ductile–brittle response of a viscoelastic medium to diffusion-driven bubble expansion. A sample of shear-thinning magma analogue is saturated by gas Ar under high pressure. On rapid decompression, Ar supersaturation causes bubbles to nucleate, grow, and coalesce in the sample, forcing it to expand, flow, and fracture. Experimental variables include saturation pressure and duration, and shape and lubrication of the flow path. Bubble growth in the experiments controls both flow and fracturing, and is consistent with physical models of magma vesiculation. Two types of fractures are observed: i) sharp fractures along the uppermost rim of the sample, and ii) fractures pervasively diffused throughout the sample. Rim fractures open when shear stress accumulates and strain rate is highest at the margin of the flow (a process already inferred from observations and models to occur in magma). Pervasive fractures originate when wall-friction retards expansion of the sample, causing pressure to build-up in the bubbles. When bubble pressure overcomes wall-friction and the tensile strength of the porous sample, fractures open with a range of morphologies. Both types of fracture open normally to flow direction, and both may heal as the flow proceeds. These experiments also illustrate how the development of pervasive fractures allows exsolving gas to escape from the sample before the generation of a permeable network via other processes, e.g., bubble coalescence. This is an observation that potentially impact the degassing of magma and the transition between explosive and effusive eruptions.

Keywords: volcanic conduit; analogue experiment; vesiculation; fragmentation; degassing

1. Introduction

During volcanic eruptions, the liberation of volatiles through vesiculation can generate contrasting physico-chemical behaviors of the enclosing magma. Amongst the physical changes, fast volume increase is in most decompressive cases the most relevant, generating a dramatic increase in the rate of deformation of the magma and an acceleration of the processes that often lead to an explosive eruption. Here we investigate the expansion, flow and fragmentation of magma using an analogue material which undergoes rapid vesiculation. In particular, we use a viscoelastic magma analogue to simulate the rate-dependent viscosity of magma, and we

* Corresponding author. Istituto Nazionale di Geofisica e Vulcanologia, Department of Seismology and Tectonophysics, Rome, Italy.
E-mail address: taddeucci@ingv.it (J. Taddeucci).

0012-821X/$ - see front matter © 2006 Elsevier B.V. All rights reserved.
doi:10.1016/j.epsl.2006.01.011

investigate the specific case of bubble growth driven by strong supersaturation.

Despite the long-standing acknowledgement of its central role in explosive volcanism, the investigation of nucleation, growth, and coalescence of gas bubbles in magma (magma vesiculation) is still providing new insights into eruptive phenomena. Recent examples come from three aspects of magma dynamics in volcanic conduits: flow, fragmentation, and degassing. Firstly, complex rheology controls how magma flows in volcanic conduits: the abundance, and size and shape distribution of bubbles strongly affect the rheology of magma [1–6] and its resulting flow profile in volcanic conduits [7]. Secondly, bubble growth in magma forces the liquid phase to deform differentially at small- and large-scales (i.e., around each bubble vs. up the volcanic conduit). At present it is still unclear if, during explosive eruptions, viscoelastic magma fragments in response to the small- or large-scale deformation and stress accumulation [8–10]. Moreover, total porosity, thickness of bubble walls and bubble pressure likely control magma fragmentation during both steady and unsteady fast decompression events [11–15]. Thirdly, bubble coalescence can eventually cause magma to become permeable and, via degassing, to erupt effusively instead of explosively [16–18] or less explosively [19]; coalescence and permeability also affect the final texture and emplacement mode of pyroclasts [e.g., 20].

Published experimental investigations on magma vesiculation used either silicate melts (remelted rock or synthetic) at magmatic temperature or analogues (including water, gum–rosin solutions, and silicon and other polymers) at ambient or lower temperature. The former are best suited for nucleation, growth, and coalescence experiments that involve relatively small strain and strain rates of the sample [e.g., 18,21,22] and the latter are best suited for highly non-equilibrium bubble expansion/fragmentation experiments at higher strain and strain rates [e.g., 23–26]. In particular, this last group of experiments does not aim at rigorous scaling of natural processes, but, as noted by [27], represents “a tool to identify and investigate the fundamental processes and interactions operating within the flows”. Within this frame we present a new type of analogue experiment on magma vesiculation and fragmentation that can be used to investigate many of the vesiculation-related processes mentioned above. A novel point of the experiment is the combination of a viscoelastic magma analogue, which has a rate-dependent rheological behavior more similar to magma [28], with the diffusion-driven nucleation, growth, and coalescence of bubbles.

2. Experimental techniques

2.1. Rheology of the magma analogue

Our magma analogue is a silicon polymer named “Changeable Silly Putty® ”. It is viscoelastic and solvent of Ar gas depending on pressure. We used a forced oscillation rheometer to measure sample rheology within the linear viscoelastic region of response (stress range from 150.7 to 3037.9 Pa, peak strain of 20%) at 25 °C. The polymer is shear-thinning, its viscosity η decreasing from 5×10^4 to 1×10^3 Pa s on the strain timescale 10^3–10^{-2} s, and its relaxation time τ is 0.2 s (Fig. 1). To evaluate the effect of dissolved Ar on the viscosity of the sample we measured the rate of sinking of a steel rod into the sample under high (10 MPa) and atmospheric pressure. Although we did not model the results to quantify the viscosity, only a minor increase in apparent viscosity under high pressure appeared (sinking velocity being 20% higher under atmospheric pressure than under high pressure), probably as a consequence of sample compaction. No other effect of dissolved gas on viscosity emerged.

2.2. Apparatus set-up

The experiments took place inside the Plexiglas® high-pressure chamber (volume 10^{-4} m^3, pressure up to 20 MPa) of a shock-tube apparatus (modified from [29]) (Fig. 2). Gas Ar entered in the chamber from the top so that the upper part of the sample saturated uniformly. The sample was left at room temperature under a given saturation pressure P_s for a given saturation time t_s.

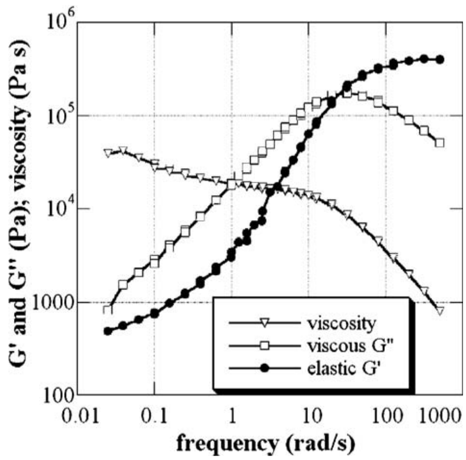

Fig. 1. The results of forced oscillation rheometry of the magma analogue at 25 °C show a shear thinning viscosity. A relaxation time of 0.2 s comes from the frequency where the elastic (G') and viscous (G'') modulus cross each other.

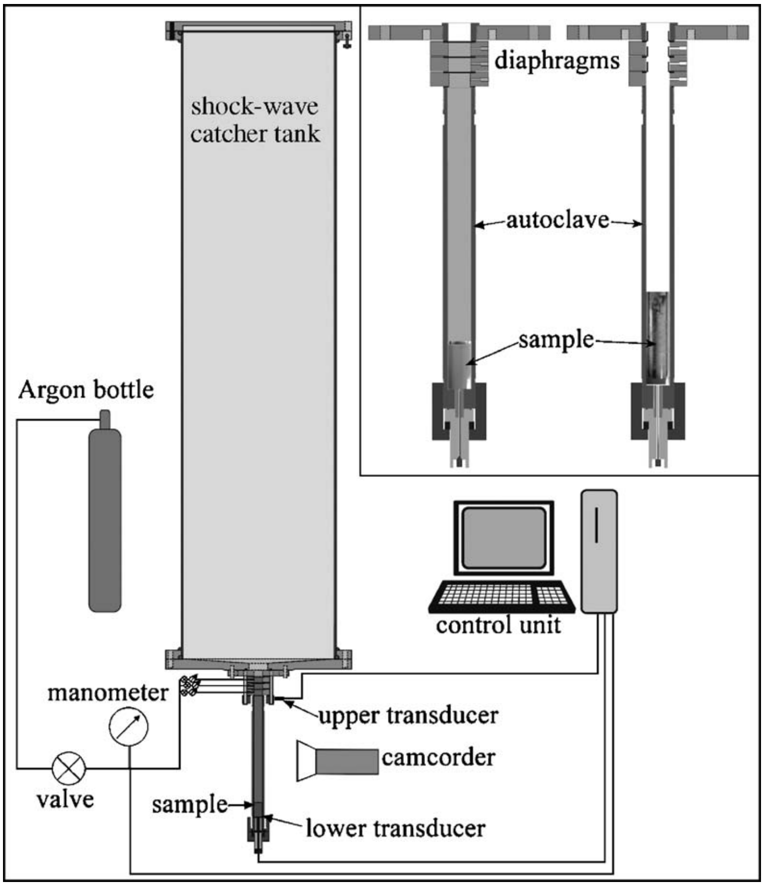

Fig. 2. Set up of the shock tube apparatus used for the experiments. In the inset, a detail of the Plexiglas® pressure chamber (inner diameter 0.02 m, outer diameter 0.05 m, length 0.4 m) and the three-diaphragms closure system before (left) and after (right) opening.

Sudden decompression of the chamber was achieved by opening a set of copper diaphragms (inset in Fig. 2). Standard (Sony DCR-TRV950, color, 25 frames per second) and high speed (Hisis 2000, black and white, up to 1220 frames per second) camcorders recorded the expansion and fragmentation of the sample, and pressure changes at the bottom and above the sample were recorded during test runs using pressure transducers (Kistler 601H). Experimental conditions (Table 1) included four variables: two of them are the pressure and time of saturation (P_s, t_s, respectively), noted above; the third is whether lubricant (glycerin) was applied or not between the sample and the chamber; and the last variable is the shape of the chamber. The "cylindrical" chamber has a uniform inner diameter of 0.02 m and length of 0.4 m, of which the lower 0.15 m ca. was initially filled with the sample (Fig. 3a). The "narrow" chamber is like the cylindrical one, but has a narrow section of diameter 0.01 m and length of 0.07 m in the middle (Fig. 3b). The initial sample head varied from below, to within, to above the narrow section.

3. Results

3.1. Overview of experimental phenomena

Upon opening the diaphragms, pressure in the chamber drops to atmospheric value, the sample is suddenly supersaturated with Ar, and bubbles nucleate and grow. Bubble growth forces the sample to expand and flow upward in the chamber (Fig. 3a). As the flow starts, contact between sample and chamber is uniform, likely provided by micron-sized bubble walls touching the chamber. During the flow, fractures open in the sample with variable geometry and timing, and, short after opening, often the fractures heal as the flow proceeds (Fig. 3b, c). After fracturing, the flow slows down and horizontal furrows develop in the sample at the interface with the chamber walls (Fig. 3d). Finally, the flow stops and, then revealing its foamed nature, collapses (Fig. 3e). Movies of representative runs are included as supplementary material to the electronic version.

Table 1
Experimental conditions and results

Run name	Chamber type *	Lubricant	P_s (MPa)	t_s (hours)	S (mm)	F_e (mm)	V_{max} (ms^{-1})	Rim fracturing	Pervasive fracturing	$1\sigma\dot{\gamma}$ (s^{-1})	X (Pa^{-1})
1	Cyl	No	9.0	12	11	106	0.26	Yes	Yes	–	–
2lub	Cyl	Yes	7.0	24	–	–	0.16	No	Gradual	–	–
3lub	Cyl	Yes	7.0	5	12	78	0.14	No	Gradual	–	–
4lub	Cyl	Yes	10.0	16	35	161	0.56	Complex	Repeated	–	–
5lub	Cyl	Yes	10.0	6	15	111	0.44	Repeated	Yes	–	–
6lub	Cyl	Yes	13.0	16	25	183	0.76	Complex	Yes	–	–
7lub	Cyl	Yes	6.0	11	12	105	0.19	Incipient	Gradual	–	–
8	Cyl	No	6.5	12	–	–	0.09	Incipient	Gradual	–	–
9	Cyl	No	4.0	21	12	60	0.12	No	Gradual	–	–
10	Cyl	No	10.7	50	–	–	0.96	Yes	Yes	–	–
11	Cyl	No	11.0	22	–	–	0.58	Complex	Yes	–	–
12lub	Cyl	Yes	11.0	23	–	–	–	Yes	Gradual	–	–
13lub	Cyl	Yes	11.0	17	–	–	0.81	Repeated	Yes	–	–
14	Cyl	No	10.5	27	–	–	0.89	Repeated	Yes	–	–
15	Cyl	No	10.3	12	19	80	1.32	Yes	Yes	8.21	0.41
16	Cyl	No	10.3	7.5	17	92	0.76	Complex	Yes	8.57	0.53
17lub	Cyl	Yes	10.2	15	20	114	0.55	Incipient	Gradual	5.70	0.56
18lub	Cyl	Yes	10.3	7.2	–	–	0.37	Incipient	Gradual	4.00	0.49
19	Cyl	No	10.3	15	18	88	0.97	Repeated	Yes	–	–
20lub	Cyl	Yes	10.2	6	13	75	0.94	Yes	Yes	6.41	0.57
21	Cyl	No	6.2	17	–	–	–	Yes	Yes	–	–
22	Cyl	No	11.1	5.7	–	–	1.35	Repeated	Yes	–	–
23	Cyl	No	10.0	340	55	–	2.17	Repeated	Repeated	–	–
23a	Cyl	No	10.0	17	18	88	0.68	Yes	Yes	5.31	0.98
24	Cyl	No	5.0	23	14	74	0.12	No	No	2.12	1.06
25	Cyl	No	5.0	6.2	9	54	0.10	No	No	2.83	1.20
26lub	Cyl	Yes	5.0	14.5	17	72	0.15	No	No	2.43	0.85
27	Cyl	No	9.8	16.3	18	129	0.73	Yes	Repeated	9.11	0.73
28	Cyl	No	10.0	5.5	13	–	0.69	Yes	Repeated	6.77	0.74
29nar	Nar	No	10.0	7.3	–	–	1.51	No	Repeated	–	–
30nar	Nar	No	10.0	15	–	–	0.48	Yes	Repeated	–	–
31nar	Nar	No	10.0	7.2	–	–	2.58	No	Fragmented	–	–
32nar	Nar	No	10.0	14	–	–	4.27	No	Fragmented	–	–
33nar	Nar	No	10.0	22	–	–	2.88	No	Repeated	–	–
34	Cyl	No	10.0	7.5	21	110	0.51	Complex	Gradual	5.12	0.52
35	Cyl	No	8.0	15	–	–	1.14	Complex	Repeated	–	–

* Cyl: cylindrical; Nar: narrowing.

To show the initial evolution of a typical run, in Fig. 4 we plot the position of the most advanced point of the flow, measured from high-speed video images, versus time. Arrival of the decompression wave causes a small upward jump of the free surface of the sample (4b), followed by detachment of the upper part of the sample from the chamber walls (4d). As soon as the bubbles start to expand, the sample surface bulges up (4e) and the whole sample starts to flow (4f). During flow, the sample fractures repeatedly, first with sharp fractures at the top that we define as "rim fractures" (4g) and later with fractures distributed throughout the sample that we define as "pervasive fractures" (4h, i, j).

From the video images we measure the length of expansion of the flow front $F(t)$ and the "saturation zone" S, i.e., the length of sample that detaches from the chamber and expands upon decompression (see Fig. 3a). Below S the sample remains unchanged throughout the experiment. We assume that S is the part of the sample where enough Ar diffused for bubbles to grow uniformly on decompression: in other words, the saturation zone is the "gas-charged" portion of the sample, and the only portion affected by the experiment. The square of S is proportional to t_s, consistent with this assumption. We can use the above proportion to estimate the diffusion coefficient D of Ar in the polymer to be on the order of 5×10^{-9} m^2 s^{-1} at 10 MPa (Fig. 5a).

F and S can be used to calculate the front velocity v, average porosity Φ, and average elongational strain rate $\dot{\gamma}$ of the flow as a function of time t, as follows:

$$v = \frac{\Delta F(t)}{\Delta t} \tag{1}$$

$$\Phi = \frac{F(t)}{F(t) + S} \tag{2}$$

$$\dot{\gamma} = \frac{\Delta F(t)}{\Delta t} \frac{1}{F(t) + S} \tag{3}$$

Below we use the above parameters and video images to detail and quantify the individual processes that characterize the experiments (Table 1).

3.2. Flowing

Upon opening the diaphragms, pressure in the chamber decreases to atmospheric value in less than 0.01 s at a mean rate of 10^9 Pa s^{-1}. Bubble expansion starts only some milliseconds after the decompression phase (Fig. 5b), and is thus entirely achieved against ambient confining pressure. Length of expansion $F(t)$ in most runs broadly follows three stages (Fig. 6a). At the beginning there is a nearly exponential increase of flow velocity, usually concomitant with the initial bulging of the sample. The duration of this stage decreases with increasing P_s. In the second stage, velocity is almost constant, except for sudden acceleration "steps" associated with fracturing episodes. Finally, with a variably marked kink, velocity drops into the third stage,

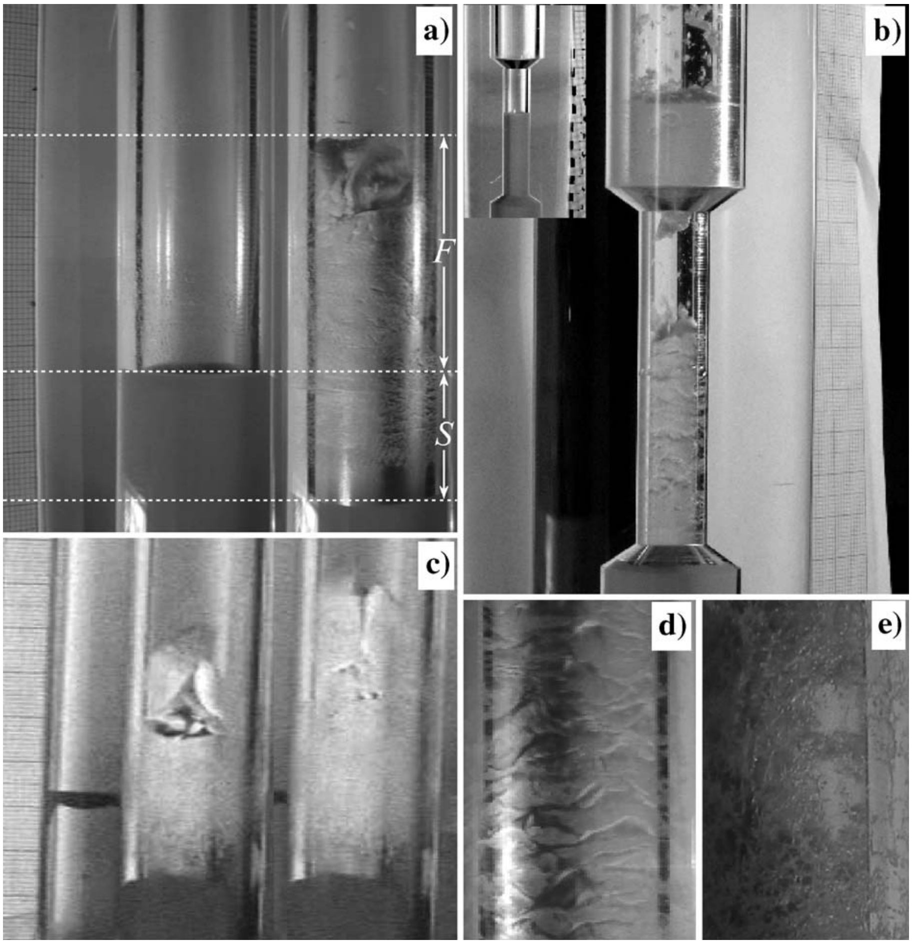

Fig. 3. Pictures of runs as various stages. a) Cylindrical chamber run 11 before (left) and during (right, t=0.12 s) expansion. In the "saturation zone" S bubbles appear to grow uniformly on decompression. F is length of expansion at time t. b) Narrow chamber run 32nar before (inset) and during expansion and fracturing. Note the large fragment filling the chamber above the narrow section and the many, smaller fragments flying above and below it. c) Cracks healing between t=0.08 and 0.012 s in run 4lub. d) Furrows at t=0.40 in run 14. e) Detail of the collapsed foam at the end of run 7lub. Smallest square in scale is 1 mm large.

characterized by the lowermost, again almost constant velocity, until the flow stops. $F(t)$ is converted into the average elongational strain rate $\dot{\gamma}$ by Eq. (3). $\dot{\gamma}$ varies markedly with varying experimental conditions (P_s, t_s, and chamber shape and lubrication) and shows a general trend of relatively fast rise followed by a more prolonged decrease. Within this trend, the first peak corresponds to the bulging, while the other peaks mark fast acceleration of the sample during pervasive fracturing (Fig. 6b). The maximum flow velocity of the sample, measured at the end of the first stage, increases with increasing P_s and, for the same P_s, with increasing t_s. Also chamber lubrication slightly increases maximum flow velocity (Fig. 6c).

3.3. Degassing

Our samples degas through vesiculation. The bubbles are too small to be observed directly with our equipment during most of the experiment, but when the flow stops the highly porous nature of the sample is evident. At the end of the experiment the foam collapses, showing that at this stage most bubbles are interconnected (see Movie 1). In the collapsed foam, visible vesicles are homogeneously millimeter-sized, mostly spherical or elongate, and occasionally irregular. Only at the bottom of the saturation zone are they smaller and more spaced. In agreement with the foamy appearance of the samples, final porosities,

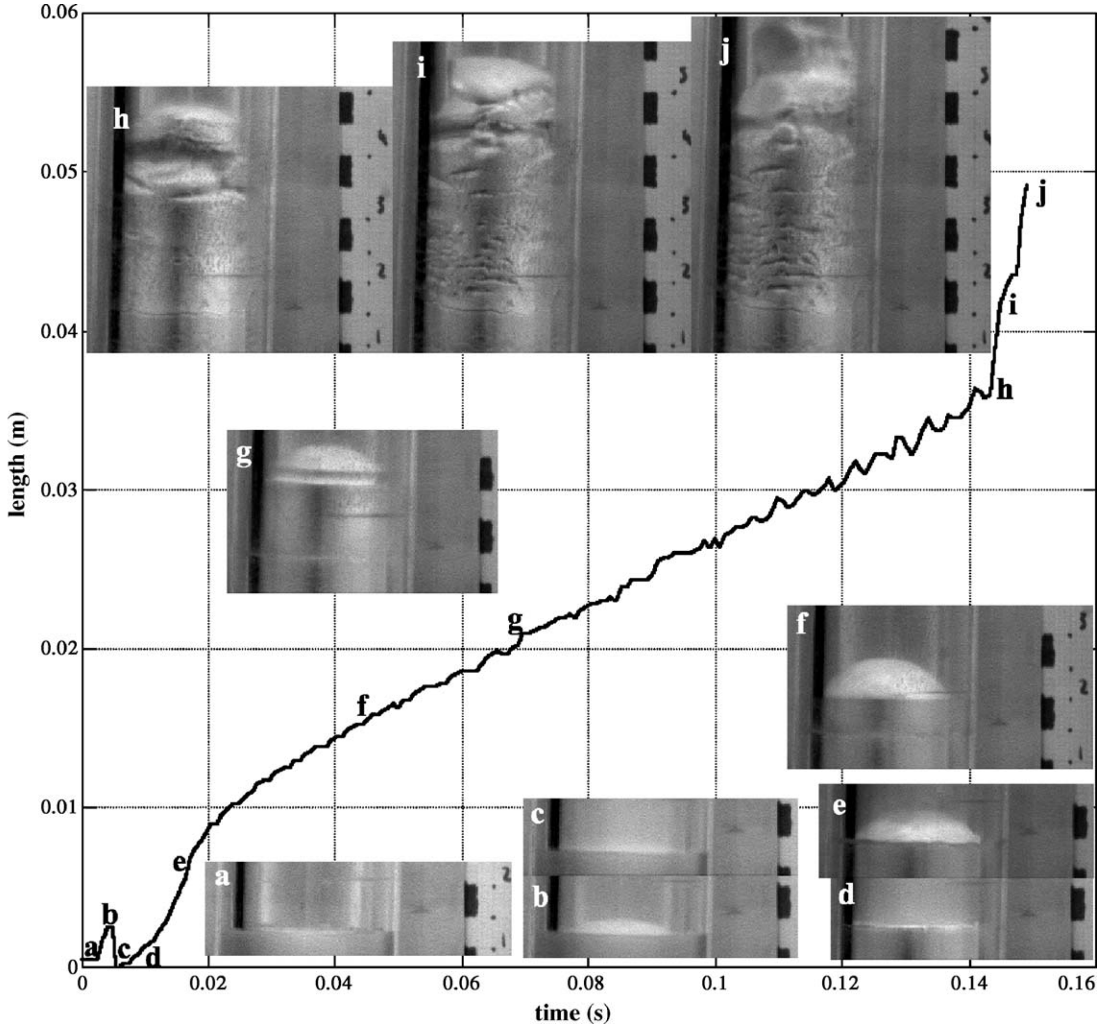

Fig. 4. Length of expansion and pictures from run 22. In (a) the sample is at rest under gas pressure; when the decompression wave arrives (b), the upper surface of the sample jumps slightly upward and then returns flat (c); between (d) and (e) the top of the sample bulges, and in (f) the sample is already expanding and flowing. Comparing (b, c) with (d, e) please note the detachment of the sample from chamber walls, most evident along the black vertical stripe on the left side of pictures. Rim fracture appears in (g) and pervasive fractures develop in (h), (i), and (j). Black rectangles on scale bar are 5 mm long in all figures.

calculated using Eq. (2), fall in the 0.8–0.9 range for almost all runs (Fig. 6d).

Occasionally, large bubbles grow and burst at the top of the flow, providing evidence for gas escape from the top of the flow, at least during the latest stages of the experiment (Movie 10). Gas pockets also escape from the sample along the interface with the chamber, both by opening their own way between sample and chamber, and by using as a pathway the furrows that form after fracturing. These gas pockets rise along the sample-chamber interface at speeds locally exceeding 10 m s^{-1} (Movie 2). Gas rising along the interface is observed to facilitate sample flow.

3.4. Rim fracturing

Rim fractures occur in the topmost part of the flow. A single, circular, sharp fracture opens in 1–2 ms perpendicularly to flow direction and cuts the bulge at the top of the flow all along its rim to a depth of ~2 mm. On opening, the fracture dips inward and downward. However, during and after fracturing expansion proceeds and the fracture changes geometry and becomes incorporated within the flow. Observed variations in rim fracturing include: 1) a fracture confined only to one side of the sample; 2) the part above the fracture overturns in the fashion of a trap-door; 3) different fracture geometry develops; 4) the fracture heals as expansion proceeds; and 5) two to four, similar fractures form in a narrow time and space interval (Table 1, see also Supplementary movies 2, 4, 6, and 10).

Which flow conditions lead to rim fracturing? All runs that underwent rim fracturing plot above the dashed line in Fig. 6a. Thus rim fractures are observed only in flows that are fast enough. It is noteworthy that rim fractures do not alter the motion of the flow. Rim fracturing does not appear in the curve of Fig. 4, flow velocity remaining unchanged before, during, and after fracturing. In search of a flow property that may correlate with the fracturing, we tracked the morphology of the flow front during several runs. Time stacks of front morphology show that, after bulging and before fraturing, the flow front develops a steeper rim including a less convex, relatively flat central plateau zone that enlarges with time (Fig. 7a,b). Front morphology can be used to extract information about flow conditions. For this purpose we measured the height of the bulge along flow direction (y) and the distance from the plateau edge to the flow margin normal to flow direction (x, Fig. 7c) as a function of time. y first increases sharply during the initial bulging of the sample, then slightly decreases as the sample starts to flow, and then increases again during

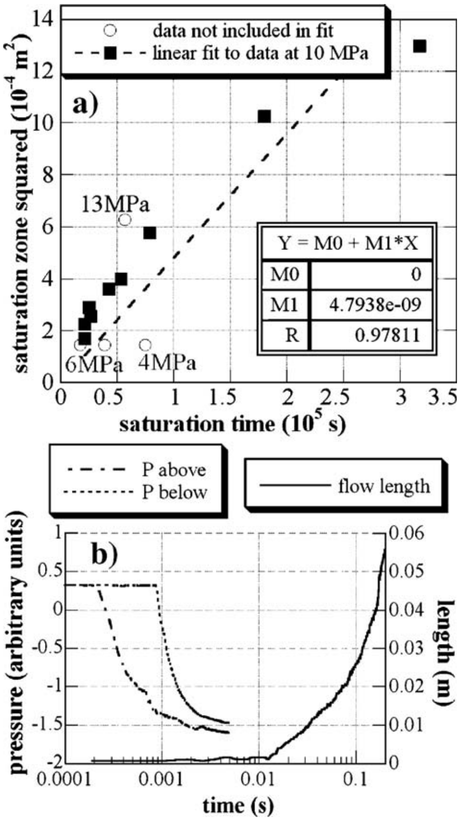

Fig. 5. a) Longer saturation time, t_s, produces larger saturation zone, S. The slope of the linear fit gives the diffusion coefficient D of Ar in the sample. D increases with increasing gas pressure. b) Pressure in the chamber above the sample and at its base (right) and length of expansion (left) as a function of time during run 4lub. The small uplift of sample surface upon arrival of the decompression wave (Fig. 4b) is used to synchronize the two data sets. The sharp drop in "P above" marks diaphragms opening. In the time lapse between the drop in "P above" and "P below" the decompression wave traveled from one transducer to the other at the speed of sound in pressurized Ar and silly putty. Pressure in the chamber is almost stable when sample expansion begin, at about 0.015 s.

the formation of the plateau (Fig. 7d). All runs follow this general trend, but with different time scales according to the different initial conditions. In particular, runs that fractured show a faster rise of y in comparison to those that did not fracture. These last ones show a decrease in y towards the end of the run, suggesting bulge deflation in the final stage of the flow. If the plateau at the flow front reflects a zone of plug flow in the flow center, we can assume that all shear strain is uniformly distributed in the zone between the plateau and the flow margin. In this case x and y can be used to calculate the shear strain rate at the flow margin $\dot{\gamma}s$ as

$$\dot{\gamma}s(t) = \frac{vy(t)}{x(t)}, \tag{4}$$

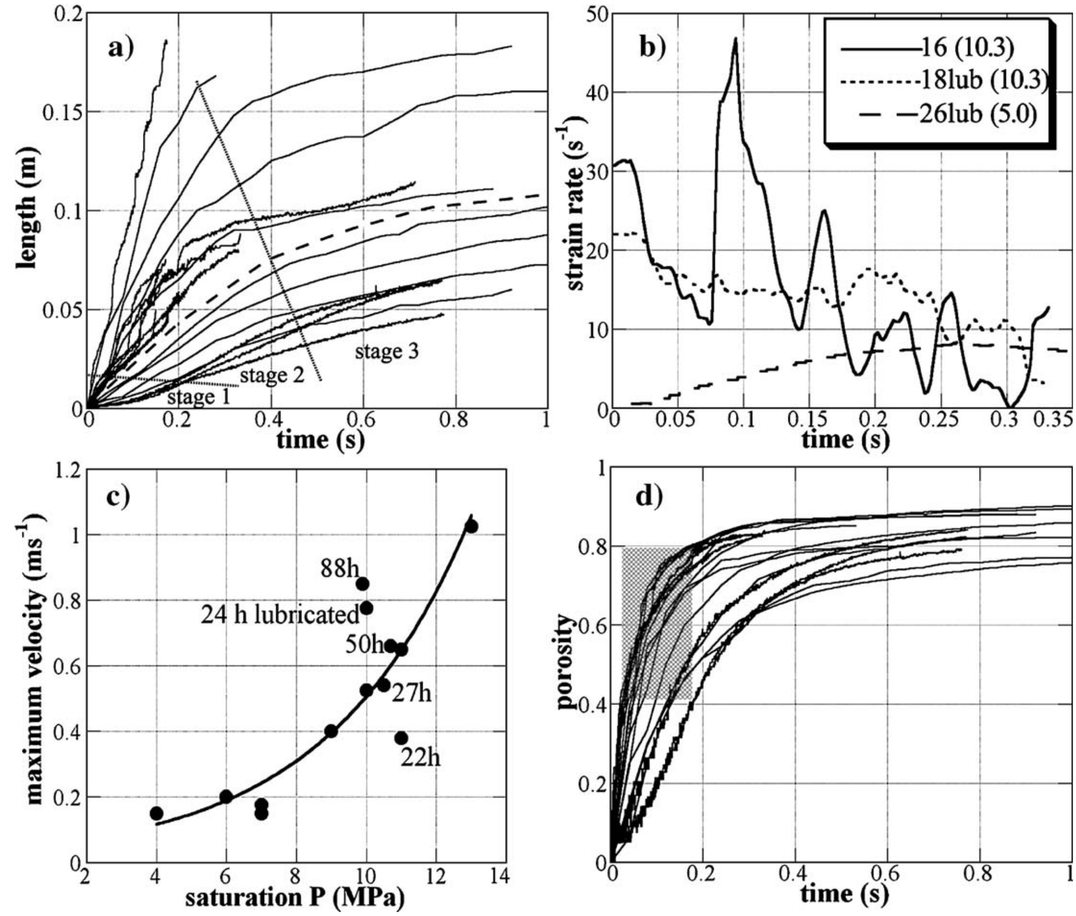

Fig. 6. a) Length of expansion in most runs broadly follows three stages with different slopes, separated by the dotted lines. Only runs above the dashed line experienced rim fracturing. b) Elongational strain rate during the first stage of three runs: 18lub and 16 are at similar conditions with and without lubricant, respectively; 26lub is with lubricant at half saturation pressure P_s (in brackets). The first peak corresponds to the initial bulging of the sample, while the following ones are due to fast acceleration of the sample during pervasive fracturing events (not occurring in run 26lub). c) Maximum flow velocity depends on P_s and, at constant P_s, on t_s. Also chamber lubrication increases flow speed. d) Porosity variations during experimental flow. The dashed area corresponds to the interval when pervasive fracturing is observed.

where the along-flow velocity differential between the plateau and the margin is

$$vy(t) = \frac{\Delta y(t)}{\Delta t}. \quad (5)$$

$\dot{\gamma}s$ increased up to 1.5–3.5 s^{-1} just before fracturing for those runs that fractured, while it reached a maximum of 0.2 s^{-1} for runs that did not fracture (Fig. 7e).

3.5. Pervasive fracturing

Pervasive fracturing usually causes a high acceleration of the flow and occurs in pulses that last tens of milliseconds. In this time, tens to hundreds of millimeter-sized fractures, perpendicular to the flow direction, open throughout centimeter-sized zones of the sample. Pulses are seldom isolated, more often occurring in swarms separated by variable time intervals and localized in adjacent zones down the sample. By this process the fractures are repeatedly displaced and distorted, usually along well-defined shear zones that cut through the sample at a well-defined angle (Fig. 8, see also Supplementary movies 2, 4, 5, 6, 9, and 10).

Pervasive fractures develop in all but the least energetic runs. However, the way in which the fractures develop varies widely as a function of boundary conditions. If the chamber walls are lubricated, fractures open later, more gradually, and, on opening, the flow accelerates less than the corresponding non-lubricated runs (Fig. 9a, Movies 3 and 5). On the contrary, the most sudden and intense fracturing, with fractures cutting the

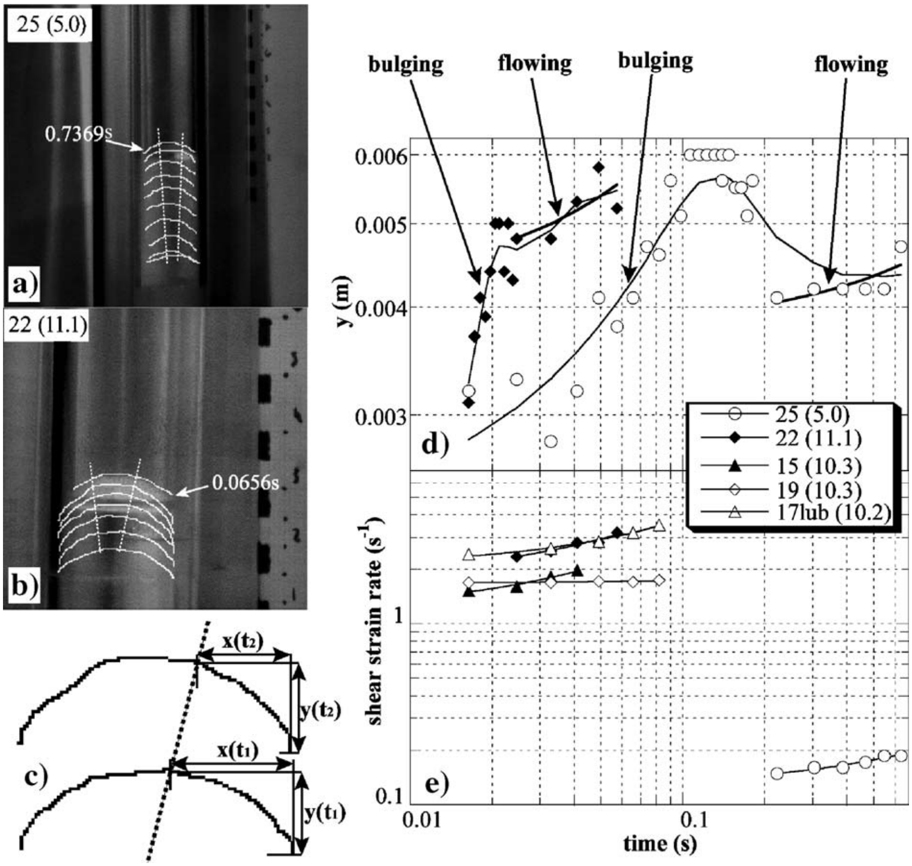

Fig. 7. a) and b) The white curves mark the shape and position of the flow front at different time intervals during runs 22 and 25, which did and did not undergo rim fracturing, respectively. Also marked is the timing of the uppermost curve (coincident with fracturing for run 22) and the development of the summit plateau zone (enclosed in the white, dashed lines). c) Geometrical definitions used to measure the flow geometry and calculate the shear strain rate at the flow margin. d) Evolution of the flow front during runs 25 and 22 (thin lines are weighted curve fits that highlight the general trend; note logarithmic abscise axis). The first rise of y marks the initial bulging of the sample before it starts to flow. As soon as flowing begins, the bulge relaxes slightly. The second rise of y coincides with the development of the plateau zone and with the time interval shown in a) and b). Thick lines are linear fits to y and provide the velocity differential used to calculate the strain rate. e) Evolution of the shear strain rate at the flow margin during five runs (note logarithmic axes). For a variety of experimental conditions, rim fracturing occurs in the 1.5– 3.5 s^{-1} interval of strain rate.

sample into pieces, occurred in runs performed using the narrow chamber. If, at the beginning of the run, the initial sample head was in the narrow portion, then the flow, on reaching the wider part of the chamber, experienced sudden expansion and acceleration, leading to sample rupture (Fig. 3b, Movies 11 and 12). It should be noted that there appears to be an inverse correlation between flow velocity prior to fracturing and the intensity of the fracturing event. Thus, in the narrow chamber run, the flow almost stops before intense fracturing and strong acceleration, while in the lubricated, cylindrical chamber run, fracturing is marked by a relatively small step in the front position plot. Another common feature of pervasive fracturing is the step-like motion it may impart to the flow (Fig. 9b). Such a motion results from pulses of fracturing that are interrupted by relatively long pauses of the flow. The duration of the pauses ranges from a few milliseconds to almost 1 s. This longest pause was observed in a run with a t_s of weeks, characterized by a saturation zone that was exceedingly large and a much prolonged phase of expansion and flow. The long expansion was not continuous but proceeded in steps, and at each step a new part of the saturation zone was observed to expand and fracture.

4. Inferences on the vesiculation and fracturing of magma

Compared with previous analogue experiments on magma flow and fragmentation, the present experiments fall dynamically between those of [25], who observed brittle fracturing but very limited deformation of a similar,

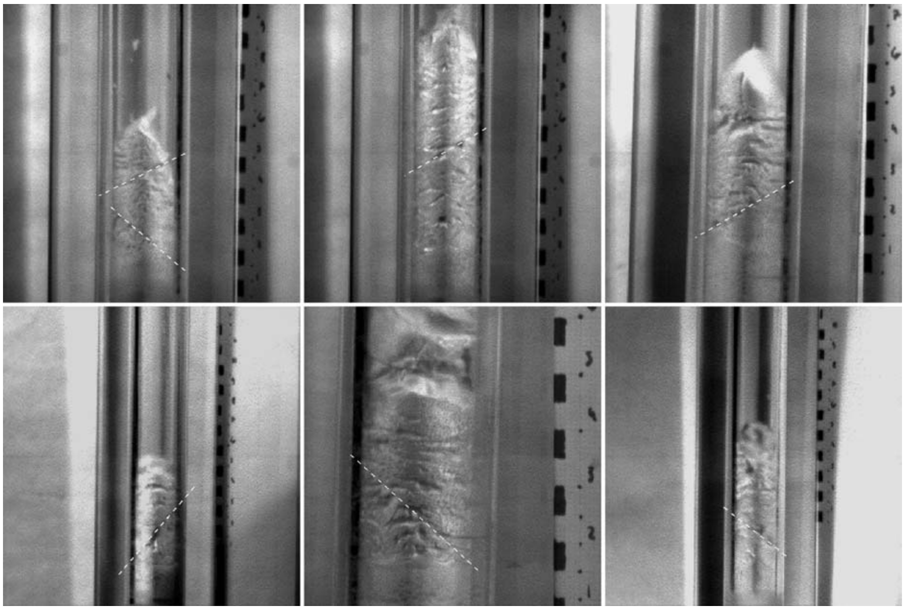

Fig. 8. Pervasive fracturing during six runs. White dashed lines mark shear zones defined by parts of the sample that fractured at different times and moved relatively to one another.

viscoelastic analogue during rapid decompression, and those of [24], showing very large and rapid expansion of the sample but involving ductile, surface-tension-controlled fragmentation of their aqueous magma analogue. The most similar experiments are those of [23] that created similar vesicularity textures during fast foaming of gum rosin–acetone solutions. As an overview of the many, significant distinctions between experiments and eruptive conduits we note the following: 1) structural diferences in materials; 2) constant vs. variable viscosity during degassing; 3) presence of a solid phase; 4) bubble growth by decompression; and 5) boundary conditions at flow edge. Perhaps one of the largest differences to keep in mind is that wall-friction seems to have a dominant role in the experiments, but both surface/volume and bubble diameter/conduit diameter ratios of the bubbly flow may be up to two orders of magnitude larger in the experiments than in volcanoes.

4.1. Vesiculation

In our experiments flow is the consequence of vesiculation, and flow velocity mainly depends on the grow rate and total number of bubbles, consistent with the results of Fig. 6c, where higher P_s, (i.e., stronger supersaturation) causes a higher number density of nuclei and faster bubble growth, while longer t_s creates a larger S and more bubbles to grow. The three stages of flow in Fig. 6a resemble those predicted by [30] for bubble growth in a supersaturated magma under constant ambient pressure. Assuming a single nucleation event in a incompressible, Newtonian liquid, they predicted bubbles to grow following three regimes, controlled initially by the viscous resistance of the liquid (viscous regime), then by the time scale for volatile diffusion (diffusive regime), and finally by the amount of volatiles left around the bubble (approach to equilibrium). Their scenario can be, at least qualitatively, applied to our case, where bubbles grow against stable, atmospheric pressure and uniform distribution of the bubbles at the end of the run suggests that only one, significant event of bubble nucleation takes place upon decompression. However, in addition to the aforementioned regimes, in our experiments the expansion profile of the sample is also affected by other processes relevant in volcanic systems, namely, wall-friction, fracturing, and gas escape. In the first stage, the expansion may be constrained not only by the viscous resistance around the individual bubbles but also by the viscous friction at the conduit wall. In the second stage, we observe variations in the expansion induced by wall-friction effects, and, instead of the smooth expansion curve expected from the diffusion model, pervasive fracturing causes the decompression and consequent expansion to propagate in steps. Gas escape, decreasing the gas available for expansion, possibly influences the second and the last stages. The sharper kink towards the last stage in the fractured vs. non-fractured runs may result from such gas escape. The fact that sample expansion tends to stop around 0.8 porosity regardless of P_s, t_s, or

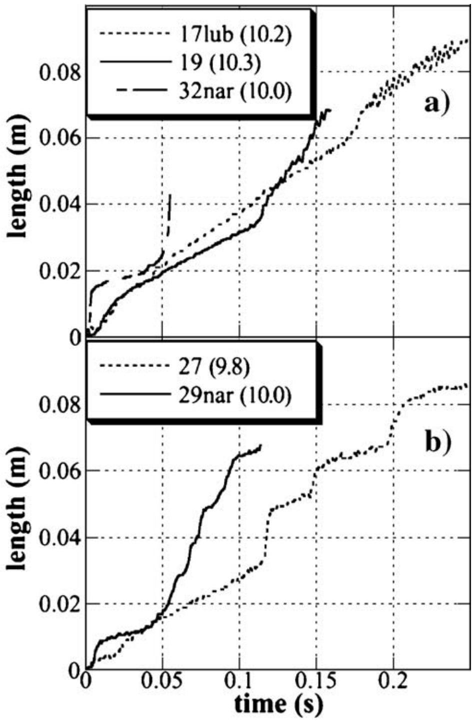

Fig. 9. a) Effect of chamber condition (lubricated, non-lubricated, and narrow) on the expansion of three runs at the same P_s and t_s. Pervasive fracturing, marked by a sudden acceleration of the flow, clearly differs between the three runs. b) Same as above for a cylindrical and narrow chamber runs, showing step-like flow motion due to repeated pervasive fracturing.

fracture history, suggests that this porosity value is an independent physical threshold. This threshold may represent a sort of "percolation" threshold where permeable gas flow prevents further sample expansion. In comparison with the ~0.8 final porosity that we observed, usual porosity of pyroclasts and predicted percolation threshold for power law bubble size distributions are around 0.7 of porosity [e.g., 14,31].

4.2. Fracturing

In the present experiments, both rim and pervasive fractures open after significant deformation of the sample and, as inferred from their features, in the brittle regime of response to deformation. Rim fractures may be related to localized shear stress annularly distributed between a central zone of plug flow and chamber walls. This is suggested by a) the fact that the fractures do not propagate throughout the flow but are confined to the rim, b) the dipping of the fractures towards the center of the flow (Fig. 4g), in agreement with a flow-parallel shear stress that induces tensional fractures in a direction normal to the minimum normal stress, and c) the localization of the fractures at the top of the flow, where flow velocity is maximum and also horizontal velocity differentials are highest due to the presence of the free upper surface. Opening of the fractures releases the stress, reduces friction, and allows the flow to proceed.

Fracturing of a viscoelastic medium requires two conditions: first, local stress must overcome the strength of the material; second, stress accumulation must be faster than stress dissipation by viscous deformation. Given that the velocity, and thus the total shear stress associated with the flow, is constant, either the sample gets weaker with time, or the stress gets more focused in a shorter time. Actually, both conditions are approached in the experiment as the flow proceeds. On the one hand, as the porosity of the sample increases thinner and thinner bubble septae must withstand the stress and the overall strength decreases. On the other hand, stress focusing at the edge of the flow manifests itself in the development of the plateau zone at the flow front and the associate increase in the shear strain rate at the flow margins (Fig. 7). Being shear-thinning, the sample is less viscous where the shear rate is higher, i.e., at the flow boundary. This localized decrease in viscosity further increases the local strain rate in a positive feedback, and, as a consequence, the profile of the flow front develops a central plateau zone and a steep border zone where velocity differentials are minimum and maximum, respectively. [32] predicted a similar process to occur in magma during isothermal steady flow. The development of a plateau zone during the experiment may also be attributable to the increasing size of the vesicles: [7] expected plug flow to develop in magma as a consequence of vesicle-induced viscoelastic behavior of the flow. Fig. 7e shows that, for runs that underwent rim fracturing, both timing and shear strain rate are similar despite different starting conditions, suggesting that, in our case, stress focusing at the flow margin may be the critical factor for rim fracturing. The uppermost value of shear strain rate we measured at fracturing ($3.5\ s^{-1}$) is slightly lower than the inverse of the relaxation time of the non-vesiculated sample ($5\ s^{-1}$), the difference possibly resulting from the presence of vesicle during the experiment. To conclude, we note that [33] shows textural evidences of fractures confined to the margins of the eroded remains of a magma flow.

Contrary to rim fracturing, pervasive fracturing strongly affects the motion of the flow up to its disaggregation in fragments. We note that, all other conditions being equal, lubricated, non-lubricated, and narrow chambers runs produce different pervasive fracturing features, and fracturing is more sudden and intense when preceded by slower expansion (Fig. 9a). These observations outline the role of wall-friction and expansion rate on pervasive fracturing. Our working hypothesis is that wall-friction may retard sample expansion and thus increase bubble pressure. In fact, an unconfined sample would expand at a velocity given by the balance between diffusive gas flux into vesicles and internal viscous (and kinetic) resistance, and the same balance controls pressure in the bubbles (cf. [34], neglecting the surface tension term). If sample expansion is confined within the chamber, then wall-friction provides additional external resistance, expansion is slower, and pressure in the bubbles is higher. This is because the sample is degassing in non-equilibrium and, remaining supersaturated, gas diffusion into bubbles continues for a relatively long time. As the sample expands, 1) total surface of the flow increases and so does wall- friction, and at the same time bubble septae get thinner and total strength decreases; 2) increased wall-friction hinders expansion; and 3) reduced expansion leads to pressure increase. Fig. 9a can now be interpreted to reflect the process described above: as wall-friction increases (from lubricated to non-lubricated to narrow chamber runs) expansion is slower, pressure build-up increases, and fracturing is more sudden and intense. Build-up of bubble pressure provides the stress. In order to cause fracturing, stress must overcome the tensile strength of bubble septae faster than dissipation due to viscous flow [25]. When bubble pressure exceeds both internal and external resistance the flow suddenly advances, fractures, and bubble pressure is thus released. After fracturing and advancing of a portion of the sample, there is a local decrease in pressure and fracturing may propagate into another portion. Downward propagation of pervasive fracturing allows decompression to propagate deeper in the sample in waves, imparting to the flow a step-like motion (Fig. 9b). The different portions of the flow move relatively to one another along the shear zones visible in Fig. 8. These shear zones are similar to those that [35] observed in pumice and explained as the result of “shear deformation …… occurring in the domain of viscoelastic response of the magma just prior to fragmentation”.

It is difficult to set a clear threshold for pervasive fracturing: due to the complex interplay between porosity, wall-friction, bubble pressure, and strength of the flow, it may occur in a relatively broad range of conditions and it ranges from sudden disruption of the sample to relatively prolonged formation of a number of fractures.

5. Further inferences on eruptive conduit processes

During experimental flow, rim fractures accommodate the local velocity differentials and cause the shear strain rate at the flow margin to drop. At this point the sample relaxes, shifting back to ductile behavior, and the fractures starts to heal. [34] describes how cycles of fracturing and healing in a rhyolitic magma produced tuffisite textures and flow banding, and shows that this mechanism may explain hybrid earthquakes observed during effusive silicic eruptions. They attribute the cracking to shear stress at the conduit margins. In our transient experiments the process cannot repeat itself for long, but during steady-state eruptions, cycles of cracking and healing could occur in magma, providing the fractures do not cut through the whole flow and gas may escape. This may also be an effective way to degas the foam without forming pyroclasts, finally leading to a vesicle-poor, degassed melt [33]. Also the occurrence of furrows at the magma margins may contribute to magma degassing. The presence of furrows in magma would also be important for flow models, as they greatly reduce the direct contact between flow and conduit. The furrows show the general aspect of fractures but develop more gradually and last longer. We hypothesize that they form when friction at the flow margin promotes bubble coalescence. Since the autoclave is impermeable to gas, gas accumulation along the interface acts as a lubricant, reducing the boundary friction of the flow. We suggest that, depending on the permeability of wall rocks to gas phases, and considering that rough conduit walls may strongly enhance local degassing at the flow margins, the same “gas-lubrication” may occur during eruptions.

An important outcome of our experiments is that fracturing enhances gas escape more efficiently than vesiculation. This outcome can be intuitively deduced from Fig. 6a where, despite the similar value of final porosity, sample expansion drops off (transition from expansion stage 2 to stage 3) earlier in runs that experienced intense pervasive fracturing. In order to provide a more rigorous determination of the above effect, we quantified pervasive fracturing and sample degassing as follows.

Pervasive fracturing causes the flow to advance suddenly, leaving a marked spike in the elongational strain rate versus time plot (Fig. 10a, b): we make use of these spikes and use the standard deviation of the strain rate as a proxy for pervasive fracturing. Then we note that all runs reach a similar value ($\sim$ 0.8) of final porosity. Fig. 10c shows a strong inverse correlation between the fracturing and the time required to reach final porosity, i.e., runs that experience more fracturing (higher strain rate standard deviation) take less time to reach the final porosity. This observation implies that pervasive fracturing allows gas to escape from the sample earlier and faster than bubble growth.

It is also useful to show how fracturing reduces the amount of gas available for bubble growth.

The total amount of gas initially dissolved in the sample (M) is a function of the solubility of gas and the volume of the gas-charged portion of the sample $S(P_s, t_s)$:

$$M = Ak(P_s - P_{amb})S, \tag{6}$$

where A is the cross-section of the sample, k the solubility coefficient of Ar in the sample (assuming that solubility follows Henry's law), and P_{amb} is the final, ambient pressure of the run. Under isothermal expansion, the final volume V of the vesicular sample would be

$$V = \frac{MRT}{P_{amb}} \tag{7}$$

where, and R and T are the gas constant of Ar and experimental temperature, respectively.

V can be compared with the final volume attained by each run, given by the final expansion length of each run F_e times A: if all the gas initially dissolved in the sample entered in the bubbles, then $F_e = V/A$. Combining Eqs. (6) with (7) for V, and under the approximation that $P_s >> P_{amb}$, we have

$$F_e = \frac{kRTP_sS}{P_{amb}} \tag{8}$$

Considering k, R, T, and P_{amb} to be constant for all runs, one can define a parameter X (Table 1) relating the initial gas content to the final expansion of the sample:

$$X = \frac{F_e}{P_sS} \tag{9}$$

If the assumption that all the dissolved gas promotes bubble growth holds, X should be constant for all runs: if otherwise, smaller values of X indicate that a smaller fraction of the gas contributed to bubble growth. On the one hand, X shows a general inverse correlation with standard deviation (Fig. 10d), meaning that the more pervasive fracturing occurred, the more gas escaped from the sample without contributing to bubble growth, and, moreover, in the shorter time, as indicated by Fig. 10c. On the other hand, X does not correlate with the final porosity reached by each run, suggesting that gas escape is not

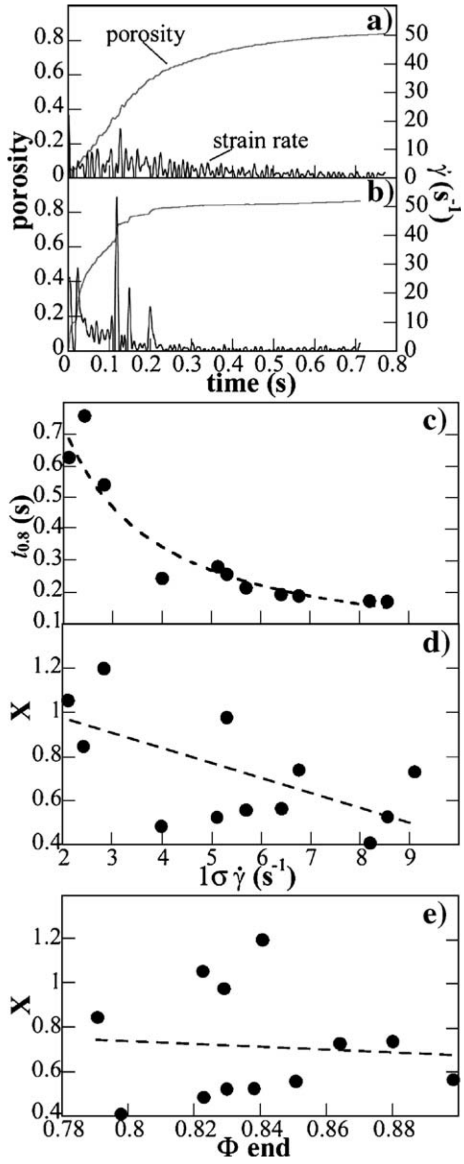

Fig. 10. Porosity and elongational strain rate during runs 25 (P_s 5.0 MPa) (a) and 27 (P_s 9.8 MPa) (b). Strain rate spikes in (b) mark pervasive fracturing events. Data filtered with a corner frequency of 100 Hz. In (c, d) we use the standard deviation of strain rate (1σ strain rate) as a proxy for pervasive fracturing. (c) The time required to reach a porosity of 0.8 ($t_{0.8}$) decreases with a power law ($R = 0.95$) as 1σ strain rate increases, indicating that expansion and degassing occur more rapidly by fracturing than by vesiculation solely. (d) X is the ratio between the final expansion of each sample (F_e) and its initial gas content (P_sS, see text for additional explanation). Smaller X indicates that a larger portion of the gas initially dissolved in the sample escaped without contributing to bubble growth. X inversely correlates (linear fit, $R = 0.60$) with 1σ strain rate (d), but does not correlate (linear fit, $R = 0.06$) with the final porosity reached by runs, Φ end (e).

a consequence of increased, porosity-related permeability (Fig. 10e). Therefore one can conclude that pervasive fracturing efficiently promoted gas escape and prevented the complete fragmentation of the sample.

6. Conclusions

Vesiculation experiments with a viscoelastic magma analogue illuminate some of the processes that previous models theorize to occur in magma flowing along an eruptive conduit. In particular, the experiments outline the potential role of friction between magma and conduit walls in controlling the motion, fragmentation, and degassing of the magmatic flow. We observe the following processes relevant for volcanic eruptions: i) brittle fracturing repeatedly interrupting ductile flow; ii) rim fracturing of the margins of the flowing, vesiculating magma analogue, due to focusing of shear stress in response to shear-thinning rheology of the analogue; iii) pervasive fracturing of the sample that releases pressure built-up due to internal (viscous) and external (frictional) resistance to expansion; iv) healing of both types of fracture as the sample keeps on flowing; v) gas escape from the vesicular flow in response to pervasive fracturing, v) preferential degassing of the sample along the flow boundary reducing wall-friction.

Acknowledgements

This paper benefited from fruitful discussions with Hugh Tuffen, Ulli Küppers, Betty Scheu, Basti Müller, and Jon Castro, and inspiring comments from Ed Llewellin and an anonymous reviewer. Alfonso Fernández Davila (a.k.a. Fon) and Ben Kennedy (a.k.a. Benutzen) provided substantial help in and out of the laboratory. Prof. Nikolai Petersen of the Geophysics Section, LMU, kindly provided the high speed camera, and Prof. Nino Grizzuti of the University of Naples “Federico II” gently provided the forced oscillation measurements. JT is supported by a Marie Curie Fellowship of the European Community program “Improving the Human Research Potential and the Socio-economic Knowledge Base” under contract number HPMF-CT-2002-01670.

Appendix A. Supplementary data

Supplementary data associated with this article can be found, in the online version, at doi:10.1016/j.epsl.2006.01.011.

References

[1] N. Bagdassarov, D.B. Dingwell, A rheological investigation of vesicular rhyolite, J. Volcanol. Geotherm. Res. 50 (1992) 307–322.
[2] D.J. Stein, F.J. Spera, Rheology and microstructure of magmatic emulsions: theory and experiments, J. Volcanol. Geotherm. Res. 49 (1992) 157–174.
[3] M. Manga, J. Castro, K.V. Cashman, M. Loewenberg, Rheology of bubble-bearing magmas, J. Volcanol. Geotherm. Res. 87 (1998) 15–28.
[4] A.M. Lejeune, Y. Bottinga, T.W. Trull, P. Richet, Rheology of bubble-bearing magmas, Earth Planet. Sci. Lett. 166 (1999) 71–84.
[5] D.J. Stein, F.J. Spera, Shear viscosity of rhyolite–vapor emulsions at magmatic temperatures by concentric-cylinder rheometry, J. Volcanol. Geotherm. Res. 113 (2002) 243–258.
[6] E.W. Llewellin, H.M. Mader, S.D.R. Wilson, The rheology of a bubbly liquid, Proc. R. Soc. Lond., A 458 (2002) 987–1016.
[7] E.W. Llewellin, H.M. Mader, S.D.R. Wilson, The constitutive equation and flow dynamics of bubbly magmas, Geophys. Res. Lett. 29 (2002) 2170.
[8] D.B. Dingwell, Volcanic dilemma: flow or blow? Science 273 (1996) 1054–1055.
[9] P. Papale, Strain-induced magma fragmentation in explosive eruptions, Nature 397 (1999) 425–428.
[10] Y. Zhang, A criterion for the fragmentation of bubbly magma based on brittle failure theory, Nature 402 (1999) 648–650.
[11] A.R. McBirney, T. Murase, Factors governing the formation of pyroclastic rocks, Bull. Volcanol. 34 (1970) 372–384.
[12] C. Klug, K.V. Cashman, Permeability development in vesiculating magmas: implications for fragmentation, Bull. Volcanol. 58 (1996) 87–100.
[13] E. Kaminski, C. Jaupart, The size distribution of pyroclasts and the fragmentation sequence in explosive volcanic eruptions, J. Geophys. Res. 103 (1998) 29759–29779.
[14] H. Gaonac’h, S. Lovejoy, D. Schertzer, Percolating magmas and explosive volcanism, Geophys. Res. Lett. 30 (2003) 1559.
[15] O. Spieler, B. Kennedy, U. Kueppers, D.B. Dingwell, B. Scheu, J. Taddeucci, The fragmentation threshold of pyroclastic rocks, Earth Planet. Sci. Lett. 226 (2004) 139–148.
[16] J.C. Eichelberger, C.R. Carrigan, H.R. Westrich, H.R. Price, Non-explosive silicic volcanism, Nature 323 (1986) 598–602.
[17] A. Rust, K.V. Cashman, Permeability of vesicular silicic magma: inertial and hysteresis effects, Earth Planet. Sci. Lett. 228 (2004) 93–107.
[18] A. Burgisser, J.E. Gardner, Experimental constraints on degassing and permeability in volcanic conduit flow, Bull. Volcanol. 67 (2005) 42–56.
[19] P. Papale, Dynamics of magma flow in volcanic conduits with variable fragmentation efficiency and nonequilibrium pumice degassing, J. Geophys. Res. 106 (2001) 11043–11065.
[20] Y. Formenti, T.H. Druitt, Vesicle connectivity in pyroclasts and implications for the fluidisation of fountain-collapse pyroclastic flows, Monserrat (West Indies), Earth Planet. Sci. Lett. 214 (2003) 561–574.
[21] J.E. Gardner, M. Hilton, M.R. Carroll, Bubble growth in highly viscous silicate melts during continuous decompression from high pressure, Geochim. Cosmochim. Acta 64 (1999) 173–1483.
[22] C.C. Mourtada-Bonnefoi, D. Laporte, Kinetics of bubble nucleation in a rhyolitic melt: an experimental study of the effect of ascent rate, Earth Planet. Sci. Lett. 218 (2004) 521–537.

[23] J.C. Phillips, S.J. Lane, A.M. Lejeune, M. Hilton, Gum rosin–acetone system as an analogue to the degassing behaviour of hydrated magmas, Bull. Volcanol. 57 (1995) 263–268.
[24] H.M. Mader, E.E. Brodsky, D. Howard, B. Sturtevant, Laboratory simulations of sustained volcanic eruptions, Nature 388 (1997) 462–464.
[25] M. Ichihara, D. Rittel, B. Sturtevant, Fragmentation of a porous viscoelastic material: implications to magma fragmentation, J. Geophys. Res. 107 (2002) 2229.
[26] A. Namiki, M. Manga, Response of a bubble bearing viscoelastic fluid to rapid decompression: implications for explosive volcanic eruptions, Earth Planet. Sci. Lett. 236 (2005) 269–284.
[27] H.M. Mader, M. Manga, T. Koyaguchi, The role of laboratory experiments in volcanology, J. Volcanol. Geotherm. Res. 129 (2004) 1–5.
[28] S.L. Webb, D.B. Dingwell, Non-Newtonian rheology of igneous melts at high stresses and strain rates: experimental results for Rhyolite, Andesite, Basalt, and Nephelinite, J. Geophys. Res. 95 (1990) 15695–15701.
[29] O. Spieler, D.B. Dingwell, M. Alidibirov, Magma fragmentation speed: an experimental determination, J. Volcanol. Geotherm. Res. 129 (2004) 109–123.
[30] N.G. Lensky, V. Lyakhovsky, O. Navon, Expansion dynamics of volatile-supersaturated liquids and bulk viscosity of bubbly magmas, J. Fluid Mech. 460 (2002) 39–56.
[31] B.F. Houghton, C.J.N. Wilson, A vesicularity index for pyroclastic deposits, Bull. Volcanol. 51 (1989) 451–462.
[32] H.M. Gonnermann, M. Manga, Explosive volcanism may not be an inevitable consequence of magma fragmentation, Nature 426 (2003) 432–435.
[33] H. Tuffen, D.B. Dingwell, H. Pinkerton, Repeated fracture and healing of silicic magma generate flow banding and earthquakes? Geology 31 (2003) 1089–1092.
[34] A.A. Proussevitch, D.L. Sahagian, Dynamics of coupled diffusive and decompressive bubble growth in magmatic systems, J. Geophys. Res. 101 (1996) 17447–17455.
[35] J. Martì, C. Soriano, D.B. Dingwell, Tube pumices: strain markers of a ductile–brittle transition in explosive eruptions, Nature 402 (1999) 650–653.